https://doi.org/10.5194/essd-2026-543
Preprint. Discussion started: 4 August 2026

Geostrophic currents in the first 2000 m of the Mediterranean water column derived from Argo float data

Gasana Elysee Manimpire[1], Annunziata Pirro[1], Elena Mauri[1], Riccardo Martellucci[1], Antonella Gallo[1], Miroslav Gačić[1], Pierre-Marie Poulain[1], and Milena Menna[1]

1National Institute of Oceanography and Applied Geophysics (OGS), Borgo Grotta Gigante 42/c, Sgonico (TS), Italy

Corresponding author: E. Manimpire Gasana (emanimpire@ogs.it)

Abstract. Extending satellite-derived surface velocities to depth in semi-enclosed basins such as the Mediterranean Sea remains challenging due to complex water mass interactions, constrained passages, and sensitivity of dynamic height calculations to numerical formulation. This study presents a three-dimensional geostrophic velocity dataset for the Mediterranean Sea (10-2000 dbar, 0.5° × 0.5°), derived from Argo float hydrography over the 2001-2024 period and referenced to satellite altimetry. A specific volume anomaly formulation is adopted for relative dynamic topography, removing the dominant hydrostatic background before vertical integration and eliminating spurious deep velocity amplification inherent to conventional specific-volume approaches. The reconstructed fields resolve basin-scale gyres, boundary currents, and mesoscale eddies across the Western, Central, and Eastern Mediterranean. Validation against Copernicus Marine Service reanalysis yields root mean squared differences of ~1 cm s^{-1} above 500 dbar, decreasing to $O(10^{-3})$ cm s^{-1} at depth, with largest uncertainties in the intermediate layer (500-1200 dbar) where water mass boundaries intensify thermohaline gradients. The dataset provides an observation-based, three-dimensional complement to model reanalyses and is publicly available at https://doi.org/10.13120/q25v-q872.

1. Introduction

The Mediterranean Sea plays a vital role in regulating regional and potentially global climate systems through teleconnections, sustaining productive marine ecosystems, and facilitating human activities such as shipping and fisheries (Micheli et al., 2013; "The MERMEX Group" et al., 2011). Understanding these diverse functions requires a comprehensive and accurate interpretation of the ocean circulation on a basin-wide scale in both surface and deep layers. Although the surface currents are relatively well understood through the geostrophic approximation due to the increased amount of accurate satellite altimetry data

https://doi.org/10.5194/essd-2026-543
Preprint. Discussion started: 4 August 2026

(Alvarez et al., 2013; Farzaneh et al., 2019), the estimation of subsurface currents in three dimensions (3D) remains a complex and challenging task (Menna & Poulain, 2010; Millot, 2005).
The reconstruction of 3D geostrophic currents from combined satellite altimetry and in situ hydrographic observations has undergone significant methodological development over the past two decades. Different methods have been used to reconstruct the ocean current in 3D. However, no one has focused on the fusion of satellite altimetry and ocean water mass properties from Argo floats to reconstruct the geostrophic current. One of the earlier implementations that attempted this approach is the work of Mulet et al. (2012), who integrated satellite-derived sea surface height with synthetic thermohaline fields derived from Argo profiles and applied the thermal wind relation in z-coordinates. Although this approach provided basin-scale consistency in the Atlantic Ocean, it exhibited sensitivity to vertical data sparsity and interpolation uncertainties, particularly below 1000 m and in narrow boundary regions.

Alternative work reformulated the problem in pressure coordinates to better align with the vertical structure of Argo observations. For instance, Vigo et al. (2018) reconstructed three-dimensional geostrophic currents in the Southern Ocean by combining absolute dynamic topography with Argo-derived temperature and salinity climatology. The vertical shear was computed using the thermal wind relation, and the Relative Dynamic Topography (RDT) was obtained by integrating the specific volume ($\alpha = 1/\rho$) in pressure coordinates, where ρ is the seawater density. While this formulation improved vertical consistency relative to earlier approaches, later reassessment by Vargas-Alemañy et al. (2023) demonstrated that deep velocity magnitudes in certain regions were sensitive to hydrographic biases and limited vertical sampling due to the Argo data limitation and dependence on the interpolation.

Even though this method performs well in some locations, it also has limitations. A key limitation of the absolute α integration-based method is that the dynamic height integral accumulates a large background hydrostatic component. In gridded hydrographic fields, even weak interpolation inconsistencies can imprint small spatial variations on this background term. When horizontal derivatives of dynamic height are taken to compute geostrophic velocities, these small variations may be amplified, particularly at depth, where the signal-to-noise ratio is reduced. This mechanism can lead to unrealistically large deep velocity estimates.

In the regional seas such as the Mediterranean Sea, which is characterised by complex bathymetry, and dynamically constrained passages such as the Strait of Gibraltar, the Sicily Channel, and the Strait of Otranto, these sensitivities are prone to significant amplification. In addition, water-mass contrasts like the Levantine Intermediate Water (LIW), Mediterranean Deep Water, and Atlantic Water (AW) can lead to an increase in the uncertainties from finite difference methods and using estimated mean properties. A preliminary Mediterranean implementation (Manimpire Gasana, 2024) adopted the Vigo et al. (2018)

https://doi.org/10.5194/essd-2026-543
Preprint. Discussion started: 4 August 2026

framework at 1° × 1° resolution; however, deep-layer velocities were found to be highly sensitive to the RDT formulation and hydrographic sparsity.

The present study introduces a mathematical refinement in the computation of the RDT. Instead of integrating the absolute αdynamic height, dynamic height is computed using the specific volume anomaly $\delta = \alpha - \alpha_0$, where $\alpha_0$is the specific volume at conservative temperature of 0 °C, absolute salinity of 35 g kg$^{-1,}$ and pressure, and it is defined from TEOS-10 (McDougall & Barker, 2011). By removing the large background component before vertical integration, this reformulation reduces the amplification of spurious deep gradients and yields depth-decaying velocity magnitudes consistent with expected Mediterranean deep-circulation measurements. As this method is based on the specific volume anomaly, it will be referred to interchangeably as the anomaly-based approach.

The refined framework combines satellite-derived absolute dynamic topography (ADT) data with in-situ salinity (S) and temperature (T) profiles obtained from Argo floats spanning the period 2001 to 2024. The reconstruction is performed on 200 vertical levels with 10 dbar spacing and covers the Mediterranean basin at a spatial resolution of 0.5° × 0.5°. To evaluate the performance of the reconstructed 3D currents, the results are compared with operational reanalysis products of T, S, and velocity currents provided by the Copernicus Marine Environment Monitoring Service (CMS). This comparison serves to assess the accuracy of the reconstruction of well-known features in the Mediterranean Sea that are identified in Fig. 1, and identify areas for possible improvements, following the approach of Rio et al.(2014). broader impact on global climate dynamics.

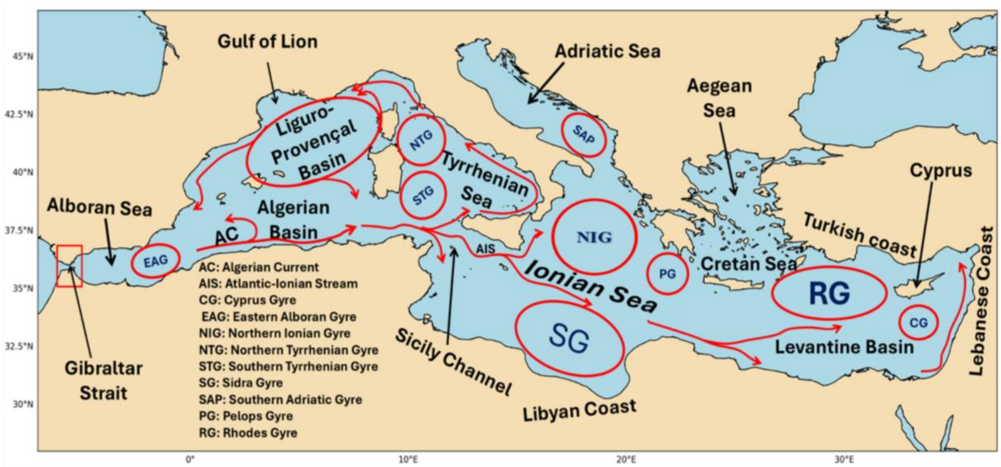

Figure 1. Annotated map of the Mediterranean Sea illustrating the major circulation features and geographic sub-basins. Red contours highlight prominent mesoscale structures, including gyres and eddies,

while curved arrows show the main surface circulation pathways. Labels identify key geographic features, including straits, marginal seas, basins, and coastal boundaries.

The reconstructed velocity field datasets are publicly released, offering a valuable resource for future investigations into Mediterranean circulation. By filling existing gaps in observational coverage and improving the accuracy of 3D geostrophic current estimates, this study contributes to a better understanding of the Mediterranean Sea's role in regional ocean processes and its broader impact on global climate dynamics.

2 . Data and Methods

To reconstruct three-dimensional geostrophic currents (Vg) across the Mediterranean Sea, an integrated methodology leveraging multi-platform observations and dynamical constraints was developed. By convention, the observations of T and S were converted into conservative temperature (Θ) and absolute salinity (S_A), respectively, by using the Sea Water Toolbox (McDougall & Barker, 2011) to produce more accurate ocean current estimates. The following sections detail the data sources, sampling strategies, processing techniques, and the reconstruction framework employed in this study.

2.1 Argo Data

Thermohaline properties of the Mediterranean Sea were examined by using vertical profiles of T and S collected by Argo floats (Wong et al., 2020). The physical data were processed and quality-controlled in delayed-mode (Wong et al 2003; Owens and Wong 2009, Cabanes et al 2016, 2021) for T and S to exclude potential sensor drift. After 2021, we used the real-time quality mode product available at the Argo Data Assembly Centre.

The data were collected across multiple pressure levels, ranging from approximately 4 dbar to 4000 dbar, with a non-uniform vertical resolution. In total, the dataset comprises about 13.5 million profiles. To investigate the spatial and seasonal distribution of the available observations, the Mediterranean Sea was divided into three basins (Fig. 1a), following the regional classification proposed in Menna et al. (2022): the Western Mediterranean basin (WMED), Central Mediterranean basin (CMED), and Eastern Mediterranean basin (EMED). This Fig. 2a subdivision was used to select an appropriate binning of the dataset, taking into account the spatial and temporal density of the data.

The WMED generally shows more consistent coverage, while the CMED reveals strong spatial variability with some highly sampled areas (Fig. 2a). The EMED is comparatively more sparsely sampled overall, though a few localized regions exhibit moderate to high data density. Coastal zones and some southern areas appear less sampled than offshore regions. Sampling effort has increased substantially over time in all three subregions (Fig. 2b). The WMED consistently contributes the largest share of profiles, followed by the CMED, with the EMED contributing the least. Peak sampling occurs in the mid-to-late 2010s, after which the effort remains relatively high but variable.

Seasonal distribution of profiles is fairly balanced, with a slight increase in spring and winter. The WMED dominates in all seasons, while CMED and EMED contributions remain smaller but relatively stable (Fig. 2c) throughout the year.

This uneven seasonal and spatial distribution is relevant for the estimation of geostrophic currents, since the method relies on horizontal gradients of T and S. In areas with limited observational density, these horizontal gradients computed after interpolation and gridding are subjected to larger errors. This limitation is particularly relevant for the Sicily Channel, a narrow and dynamically active region that controls the exchange between the WMED and EMED and hosts circulation features such as the Atlantic Ionian Stream (Poulain et al., 2012; Menna et al., 2019; Napolitano et al., 2025). Consequently, while the dataset provides sufficient coverage for basin-scale analysis, local comparisons between Argo-derived fields and CMS products in sparsely sampled regions and seasons should be interpreted with consideration of the observational density.

The original Argo observations were organised on a regular horizontal grid with a spatial resolution of 0.5° × 0.5° and interpolated vertically using linear interpolation to regular pressure levels from 10 to 2000 dbar with a vertical spacing of 10 dbar. This regridded dataset was aggregated to produce daily means, enabling the estimation of root mean squared error, bias, and standard error between Argo and CMS data by counting and averaging measurements within each grid cell and depth level over the 24 years.

However, for the computation of the long-term mean, averaging was first performed separately for each year to account for interannual variability in profile availability. The final time-averaged mean was then computed as a profile-count-weighted average, $y_M = \sum_{i=1}^{N} \frac{n_i}{n_T} y_i$ where n_T is the total number of profiles across all years in that grid cell and level n_i denotes the number of profiles in a given grid cell and level during year i, while y_i is the corresponding yearly mean. This weighting ensures that years with higher observational coverage contribute proportionally more to the long-term mean, thereby reducing biases introduced by uneven temporal sampling.

https://doi.org/10.5194/essd-2026-543
Preprint. Discussion started: 4 August 2026

The resulting weighted time-averaged field has dimensions of 200 vertical levels, 36 latitudinal points, and 86 longitudinal points.

2.2 Quality Control of Argo Data and Reconstruction of Hydrographic Fields

A multi-step quality control (QC) and reconstruction procedure was applied to remove erroneous data and reconstruct missing values from Argo data while preserving physically realistic gradients. The following steps were taken to quality-control the dataset: observations falling outside the regional limits typical for the EMED (S_A between 35 and 42 g kg^{-1}; and Θ varying between 11.5 and 35 °C) were discarded. Next, all land points were identified by using a 3D mask, with land values set to NaN to prevent contamination during interpolation and filtering. The density stability was then analysed. First, the density (ρ) was calculated as a function of S_A, Θ and pressure (P) using the GSW Python package (https://www.teos-10.org/). Layers exhibiting static instability ($\frac{\partial \rho}{\partial P} < 0$) were flagged and vertically interpolated to maintain monotonic density profiles (Jackett & McDougall, 1997; Millero & Poisson, 1981). Short vertical gaps in profiles (fewer than six consecutive levels) were linearly interpolated, whereas larger gaps were left unfilled to avoid introducing artificial structure. Subsequently, the horizontal background field was corrected: basin-scale background medians were computed using a 3-by-3 moving window, and individual profiles were blended with these background estimates to stabilize regions with sparse sampling. Each vertical profile was then smoothed using a 5-point boxcar filter, as explained in Foucher & Lopez-Martinez (2014), to suppress high-frequency noise and preserve the structure of thermocline and halocline gradients. After reconstruction, a Gaussian filter with standard deviation (σ) of 0.6 was applied to the S_A and Θ fields to remove small-scale noise while preserving mesoscale structures (Lermusiaux, 2006), and the same filtering was later applied to the velocity fields. Finally, a top-layer completeness check and inpainting were performed: columns lacking near-surface data (first valid level deeper than 50 dbar or more than three levels from the surface) were identified and filled horizontally using nearest-neighbour interpolation.

2.3 CMS Data

Profiles of potential temperature and salinity of the CMS Mediterranean reanalysis product (MEDSEA_MULTIYEAR_PHY_006_004) were used to compare with the S and T from the Argo floats. They were downloaded from https://data.marine.copernicus.eu/product/MEDSEA_MULTIYEAR_PHY_006_004/description. This product is generated using the NEMO ocean model combined with a variational data assimilation scheme (OceanVar), which incorporates in-situ T and S profiles, including Argo float observations, as well as satellite altimetry data. The dataset has a spatial resolution of 0.042 ° x 0.042 ° and a daily temporal

https://doi.org/10.5194/essd-2026-543
Preprint. Discussion started: 4 August 2026

resolution. The data were extracted over the same time range as the Argo dataset and converted into S_A and Θ. Next, the profiles were linearly interpolated to the regular pressure levels from 10 dbar to 2000 dbar, similar to the pressure levels in the Argo data, and then time sampling was done to select the data on the same days as the Argo dataset. The resulting data were then interpolated to the spatial coordinates (longitude and latitude) of the Argo float using the nearest neighbor technique. This produced a CMS dataset with the same shape as the Argo dataset in time and space. The resulting dataset was projected to the regular grid with a targeted spatial resolution of 0.5 ° x 0.5 °. Hereafter, any estimated quantity from this dataset in this study will be referred to as CMS.

2.4 Surface Altimetry Data

The ADT used in this study was obtained from CMS. This altimetric product with a spatial resolution of 0.125 ° x 0.125 ° and daily temporal resolution was processed by the Data Unification and Altimeter Combination System (DUACS) multi-mission altimeter data processing, and it is available at https://doi.org/10.48670/moi-00141. To align this dataset with the Argo float data, the ADT was remapped onto a grid with a resolution of 0.5 ° x 0.5 °. To minimize the bias in the final estimation, ADT was temporally sampled based on the days from the Argo floats dataset. To minimize temporal bias, ADT was sampled at the Argo observation dates. For each spatial bin, a 24-year weighted mean was computed using the annual observation count as weights, ensuring consistency with the averaging applied to the Argo data. The spatial smoothing technique using a convolution function from the Python package scipy available at https://docs.scipy.org/doc/scipy/reference/generated/scipy.ndimage.convolve.html with a window of size 3 was also applied to the time-averaged ADT values to reduce high-frequency noise, ensuring that the data more accurately reflect large-scale geostrophic flow patterns rather than short-term fluctuations (Powell & Leben, 2004; Quilfen & Chapron, 2021). Finally, no-normal flow boundary conditions (kinematic boundary conditions) were applied to the final product to eliminate ocean current components that are normal to the coast.

2.5. The 3D geostrophic current field based on the Argo T and S dataset

Geostrophic currents along the water depth were computed combining the relative dynamical topography (RDT), derived using T and S profiles from the Argo floats, with the ADT using the following modified version of Vigo et al., 2018:

https://doi.org/10.5194/essd-2026-543
Preprint. Discussion started: 4 August 2026

$$u_g(x,y,zi) = -\frac{g(y)}{f}\left(\frac{\delta ADT}{\delta y}(x,y) + \frac{\delta RDT}{\delta y}(x,y,zi)\right) \quad (1)$$

$$v_g(x,y,zi) = \frac{g(y)}{f}\left(\frac{\delta ADT}{\delta x}(x,y) + \frac{\delta RDT}{\delta x}(x,y,zi)\right) \quad (2)$$

with

$$RDT(x,y,zi) = \frac{1}{g(y)}\int_0^{P(zi)} \left(\frac{1}{\rho(x,y,P(zi))} - \frac{1}{\rho_o(P(zi))}\right) dP'. \quad (3)$$

Where u_g and v_g are the zonal and meridional components, respectively. $P(zi)$ is the pressure at depth *zi* in Pascal (dbar), g is the gravity in m s^{-2}, ρ is the density at a given T, S, and pressure depth, ρ_o is the density at the standard temperature of 0 °C and salinity of 35 g kg^{-1} in kg m$^{-3,}$ and *f* is the Coriolis parameter. To compute ρ, the Gibbs Seawater toolbox (McDougall & Barker, 2011) was used.
First, we modified the vertical integration limits in the RDT equation by replacing the ocean bottom with a specified reference pressure level (P(z_i) dbar). Vigo et al. (2018) integrated from the ocean bottom to the surface, which requires assuming negligible bottom velocities. This assumption is problematic: both Stewart (1997) and Cocks et al. (2025) documented that bottom currents are often significant, introducing systematic errors when the ocean floor is used as a level of no motion.
Second, in the RDT equation, we used the difference between the specific volume $\frac{1}{\rho(x,y,P(zi))}$ and the standard specific volume calculated at a temperature of 0 °C and salinity of 35 g kg^{-1}, $\frac{1}{\rho_o(P(zi))}$, as broadly accepted by the scientific community (Biló et al., 2014; Doglioni et al., 2023; Green, 1984)

To ensure the physical consistency of coastal behaviours, a tangent boundary constraint was applied using cancellation of the normal component of the velocity. This enforces no-normal flow (zero cross-shore velocity) along the coastline by projecting the velocity vectors onto local coastline tangents and applying a Gaussian alongshore smoothing (σ = 1 grid cell). This approach minimizes artifact divergence near complex coastlines (Marchesiello et al., 2001).
To eliminate unrealistic deep velocities caused by sparse or noisy dynamic-height gradients, a depth-dependent velocity cap was applied to the absolute geostrophic current fields. This procedure constrains velocity magnitudes to physically realistic values that decrease with depth, consistent with observed attenuation of the mesoscale kinetic energy in the ocean interior (Ferrari & Wunsch, 2009; Wunsch, 1997).

To prevent unrealistically large subsurface geostrophic velocities and to avoid artificial vertical discontinuities in the reconstructed current field, we introduce a depth-dependent velocity cap. The cap is

https://doi.org/10.5194/essd-2026-543
Preprint. Discussion started: 4 August 2026

Earth System Science Data
Open Access Discussions

designed to reflect the surface-intensified structure of mesoscale circulation, where kinetic energy typically decays with depth.

The initial cap is defined as an exponential function of pressure:

$$V_{cap}(P) \ = \{V_{max}\, e^{-\frac{P}{1200}}, \quad P < \ 500 \; 0.5\, x\, V_{max}\, e^{-\frac{(P-500)}{700}}, P \geq \ 500 \quad (4)$$

Smooth transition via logistic blending was then applied to the estimated velocity:

$$V_{cap}(P) = w(P)V_{upper}(P) + (1 - w(P))V_{lower}(P) \quad (5)$$

If $|(u_g, v_g)| > V_{cap}(P) \quad \Rightarrow \quad u_g = u_g \frac{V_{cap}(P)}{|(u_g,v_g)|}$ and $v_g = v_g \frac{V_{cap}(P)}{|(u_g,v_g)|}$ then to enforce softening, $|(u_g, v_g)| \leq U_{99.5}$ where V_{upper} is the V_{cap} first condition and V_{lower} is the second condition, respectively, in equation (4), $|(u_g, v_g)|$is the magnitude of the geostrophic current field, $w(P) = \frac{1}{1+e^{(P-500)/50}}$ is the weight that prioritizes the first condition when pressure, P is smaller than 500 dbar, and the second condition in case of P is greater than 500 dbar, while it combines both conditions when P is close to 500 dbar. Then $U_{99.5}$ is the 99.5 percentile of the velocity magnitude $|(u_g, v_g)|$ is used rather than using this capped velocity directly.

This constraint keeps near-surface velocities close to V_{max} and abyssal velocities near 2000 dbar close to 1 cm s^{-1}. The exponential decay follows the empirical observation that mesoscale geostrophic kinetic energy decreases by one order of magnitude between the surface and 2000 dbar (Wunch, 1997). When the computed velocities exceeded $V_{cap}(P)$, they were proportionally rescaled, preserving flow direction while limiting unrealistic magnitudes. This approach serves as a physically motivated regularization, similar to dumping schemes used in other operational ocean data-assimilation systems (Guinehut et al., 2012; Mulet et al., 2012). After this process, a Gaussian filter was reapplied as mentioned above in section 2.1.

The final u_g and v_g were horizontally smoothed using a Gaussian filter with a sigma (σ) of 0.6° and restricted to ocean grid points to reduce small-scale noise introduced during gradient computation and ensure coherence with mesoscale circulation features (Arbic et al., 2013). To assess the quality of the final fields, we computed diagnostic metrics including: (i) spatial data completeness (percentage of valid ocean grid points), (ii) the fraction of profiles requiring density inversion corrections, (iii) the percentage of velocity values that exceeded the depth-dependent cap and were rescaled, and (iv) the 99th percentile of

https://doi.org/10.5194/essd-2026-543
Preprint. Discussion started: 4 August 2026

velocity magnitude to identify potential outliers.

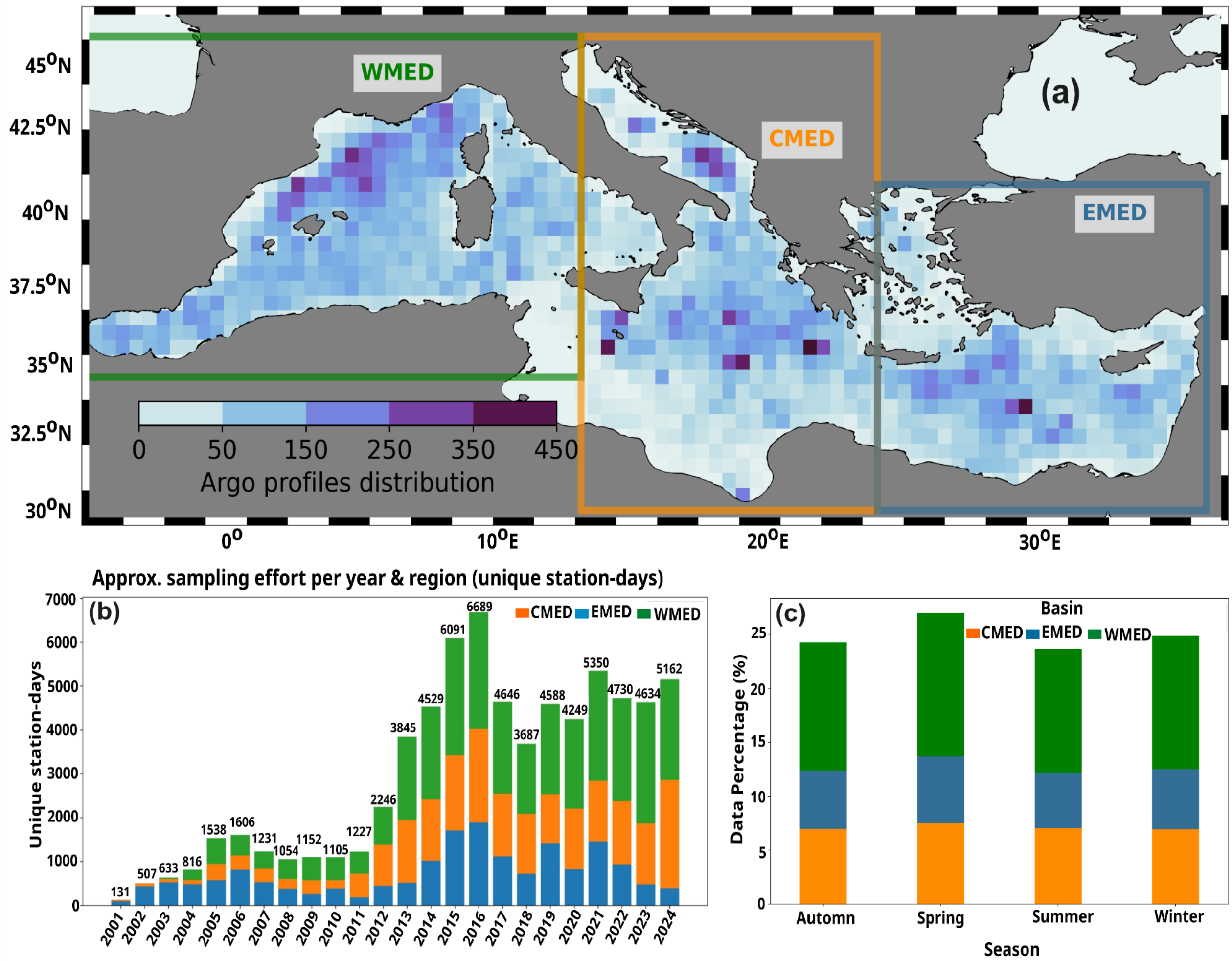

Figure 2. Yearly distribution of Argo float data collected in the Mediterranean Sea from 2001 to 2024: spatial (a), yearly (b), and seasonal (c) distributions of Argo data across the Mediterranean Sea basins (EMED, CMED, and WMED). For the spatial distribution, data points were binned at 0.5° × 0.5° resolution.

.

The output fields included reconstructed S_A and Θ, dynamic height (DH), u_g, v_g, and velocity magnitude profiles (V_{mag}).

Further analysis was conducted to identify which season contributes most to the geostrophic current estimates and which basin is most affected by the seasonal distribution, as displayed in Fig. 2c.

3. Comparison with operational model

https://doi.org/10.5194/essd-2026-543
Preprint. Discussion started: 4 August 2026

To validate the consistency of our method, the reconstructed geostrophic currents from Argo (V_g^{Argo}) were compared with the geostrophic currents derived from the CMS model (V_g^{CMS}). In addition, the total velocity field, V_{CMS_Full}, which includes both geostrophic and non-geostrophic components, was also compared with V_g^{Argo} and V_g^{CMS} to assess the depth where ageostrophic currents dominate. The comparison was done on both zonal and meridional components at the basin scale and the whole Mediterranean Sea. The V_{CMS_Full} data derived from the CMS model available at **https://data.marine.copernicus.eu/product/MEDSEA_MULTIYEAR_PHY_006_004/description** were sampled in time according to the days Argo data were present in the dataset and interpolated to the latitudes and longitudes of the Argo profiles. Afterward, V_{CMS_Full} was binned at the spatial resolution of 0.5° x 0.5°, and interpolated to the regular pressure levels using linear interpolation to match the horizontal and vertical spatial resolution used in this study. A Gaussian filter with similar parameters as used on V_g^{Argo} was also applied to the final dataset to reduce noise. During a comparison of these datasets, we evaluated the relative importance of non-geostrophic forces and cross-validated the robustness of our geostrophic estimates. Similarly, we computed the difference between S_A^{Argo} and S_A^{CMS}, and Θ_{ARGO} and Θ_{CMS} for the whole Mediterranean Sea to clarify any discrepancy in the ocean current velocity estimates as the effects of the mismatch in S_A and Θ. It should be noted that the CMS reanalysis assimilates Argo observations down to 2000 m depth, which introduces a degree of dependence between the datasets and must be considered when interpreting the validation results.

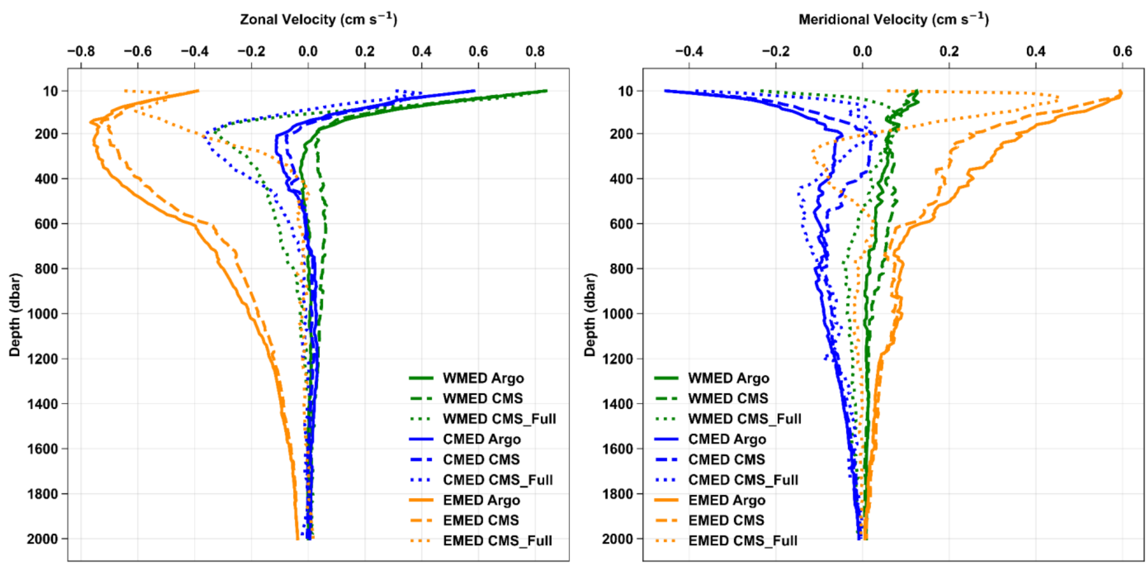

Figure 3. Basin-scale mean zonal (left) and meridional (right) velocity profiles as a function of depth (dbar) for WMED (green), CMED (blue), and EMED (orange) over the period 2001-2024. The solid lines represent V_g^{Argo}, dashed and dashed lines V_g^{CMS}, and dotted lines V_{CMS_Full}.

https://doi.org/10.5194/essd-2026-543
Preprint. Discussion started: 4 August 2026

Fig. 3 shows the vertical structure of basin-scale mean zonal (left) and meridional (right) velocity components for the WMED, CMED, and EMED over the period 2001-2024. In the zonal component (left panel), the EMED exhibits predominantly westward (negative) velocities across most depths. Near the surface (0-50 dbar), the magnitude of V_{CMS_Full} is larger than that of V_g^{Argo} and V_g^{CMS}, likely reflecting the contribution of ageostrophic processes, including wind-driven currents. With increasing depth, all components weaken.

In contrast, the WMED and CMED display eastward (positive) zonal velocities near the surface, which decrease with depth and transition toward weak westward values below ~150-200 dbar. This vertical structure is consistent with the general Mediterranean circulation, characterized by eastward transport of relatively fresh Atlantic Water in the surface layer and the westward flow of Levantine Intermediate Water at intermediate depths. The weak negative zonal velocities below ~200 dbar likely reflect the increasing influence of intermediate-layer circulation and the partial compensation between opposing flow components.

In the meridional component (right panel), all basins show a general decrease in magnitude with depth. In the EMED, V_{CMS_Full} exhibits a vertical structure with alternating northward and southward flow, with transitions around ~200 dbar and ~600 dbar. This pattern may indicate vertical layering in the circulation; however, its interpretation requires caution as it likely reflects the contribution of ageostrophic processes. In contrast, V_g^{Argo} and V_g^{CMS} show weaker and more vertically coherent meridional structures.

In the CMED, the mean meridional velocities are predominantly southward, although V_{CMS_Full} and V_g^{CMS} exhibit localized northward flow in the upper 400 dbar. This variability may reflect regional circulation features and differences in the representation of water-mass structure.

In the WMED, V_{CMS_Full} shows relatively stronger southward velocities near the surface, with magnitudes decreasing rapidly with depth. In contrast, V_g^{Argo} and V_g^{CMS} remain weak throughout the water column, with small northward values generally below 0.1 cm s^{-1}. This discrepancy in the water column (~800 dbar), where the ocean currents are mainly geostrophic, might be attributed to model adjustment and constraints in the assimilation of the observations.

The comparison between zonal and meridional velocity components derived from V_g^{Argo}, V_g^{CMS}, and V_{CMS_Full} is presented in Fig. 4, which shows bias profiles (top) and corresponding Root Mean Squared Difference (RMSD) profiles (bottom) as a function of depth for the three basins.

https://doi.org/10.5194/essd-2026-543
Preprint. Discussion started: 4 August 2026

In the zonal component (top-left panel), the EMED exhibits the largest discrepancies among datasets. The bias between V_g^{Argo} and V_g^{CMS} remains relatively small (within ±0.10 cm s^{-1}) between 200 and 1200 dbar. In contrast, larger differences are observed when comparing geostrophic estimates with V_{CMS_Full} , particularly in the upper ocean, where biases exceed 0.5 cm s^{-1} above ~150 dbar and remain elevated down to intermediate depths.

In the CMED, zonal biases between V_g^{Argo} and V_g^{CMS} are generally weak (within ±0.05 cm s^{-1}), while larger negative biases (down to -0.30 cm s^{-1}) with respect to V_{CMS_Full} occur above ~1200 dbar. A similar vertical structure is observed for the V_g^{CMS}-V_{CMS_Full} comparison.

In the WMED, the zonal bias between V_g^{Argo} and V_g^{CMS} is small, with slight positive values (~0.10 cm s^{-1}) above ~200 dbar and weak negative values below. However, larger discrepancies are again observed when comparing with V_{CMS_Full}, with biases reaching approximately -0.50 cm s^{-1} near the surface and transitioning to positive values (~0.40 cm s^{-1}) between ~50 and 1200 dbar. Below ~1000 dbar, zonal biases in both WMED and CMED tend toward zero.

In the meridional component (top-right panel), biases are generally smaller but exhibit basin-dependent structures. In the EMED, the bias between V_g^{Argo} and V_g^{CMS} peaks around 200 dbar (~0.12 cm s^{-1}) and decreases toward zero below ~800 dbar. Comparisons involving V_{CMS_Full} show predominantly negative biases in the upper ocean, which weaken with depth.

In the CMED, the meridional bias between V_g^{Argo} and V_g^{CMS} remains within ±0.10 cm s^{-1} in the upper 500 dbar but becomes positive (up to ~0.25 cm s^{-1}) at intermediate depths. In contrast, biases relative to V_{CMS_Full} are largest in the upper 400 dbar and oscillate around zero below.

In the WMED, meridional biases are modest, with values around -0.30 cm s^{-1} near the surface that rapidly decrease toward zero with depth.

The RMSD profiles (bottom panels) show consistent behavior across basins. For both zonal and meridional components, the RMSD between V_g^{Argo} and V_g^{CMS} remains low (<0.6 cm s^{-1}) and decreases with depth. In contrast, comparisons involving V_{CMS_Full} exhibit substantially larger RMSD values, particularly near the surface, reaching approximately 2.4 cm s^{-1} in WMED, 2.9 cm s^{-1} in CMED, and 3.4 cm s^{-1} in EMED, before decreasing with depth.

This enhanced mismatch in the upper ocean likely reflects the contribution of ageostrophic motions in V_{CMS_Full}, as well as differences in the underlying hydrographic fields used in the simulations. Additionally,

https://doi.org/10.5194/essd-2026-543
Preprint. Discussion started: 4 August 2026

the relatively sparse data coverage in the EMED (Fig. 2) may contribute to the larger RMSD observed in this basin.

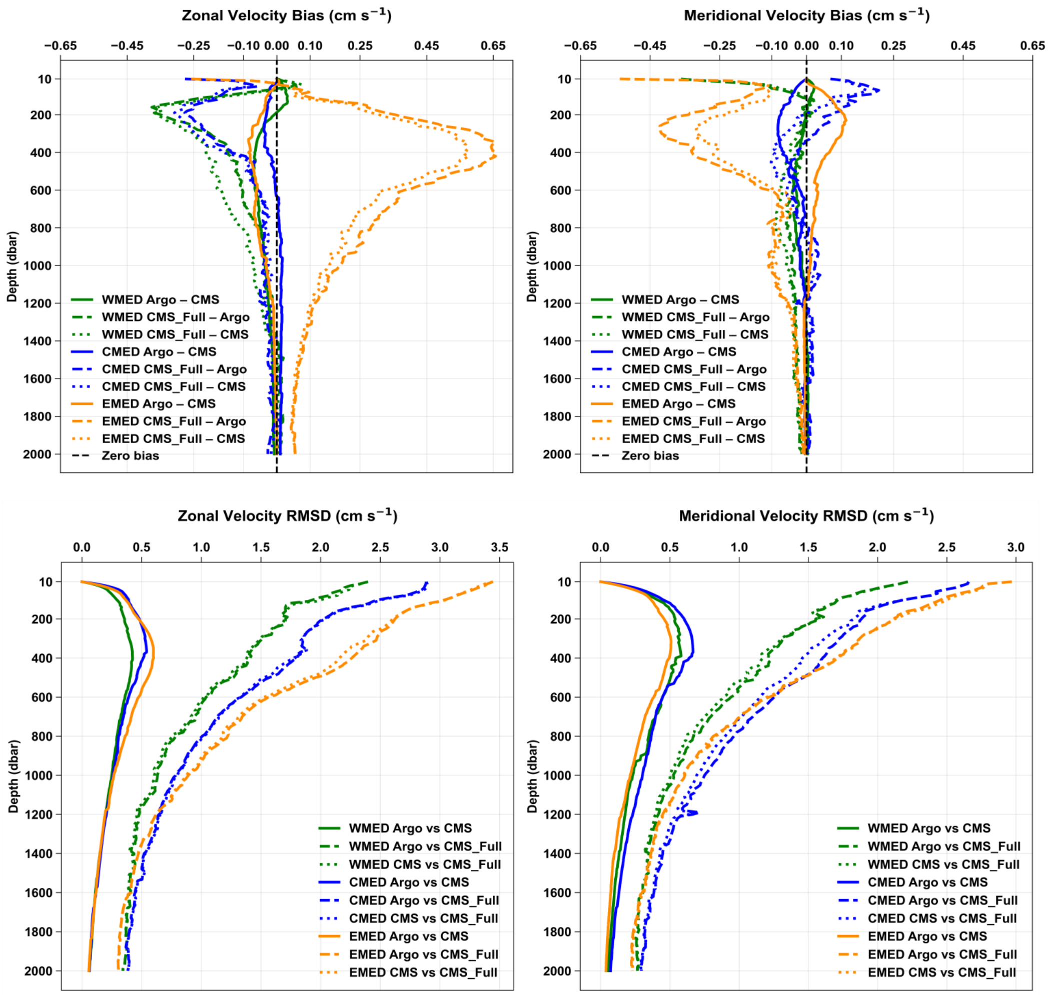

Figure 4. Basin-scale zonal (left) and meridional (right) bias (top) and corresponding RMSD profiles (bottom) as a function of depth (dbar) for WMED (green), CMED (blue), and EMED (orange). The solid lines represent V_g^{Argo}, dashed lines V_g^{CMS}, and dotted lines V_{CMS_Full}.

4. Geostrophic Velocity Maps

This section presents the main results derived from the analysis of Argo observations and their comparison with CMS reanalysis data, using the methodology described in Section 2. The results are organized to first

https://doi.org/10.5194/essd-2026-543
Preprint. Discussion started: 4 August 2026

assess the consistency between datasets in terms of estimated ocean currents, followed by an evaluation of the derived geostrophic velocity fields. To evaluate the ability of the proposed method to resolve Mediterranean circulation patterns across the water column, Fig. 5 shows horizontal geostrophic velocity fields at three representative depths (100, 1000, and 2000 dbar) together with the corresponding ${S_A}^{Argo}$ distributions.

At 100 dbar, the reconstructed geostrophic circulation reproduces the main large-scale features of the Mediterranean circulation. In the WMED, these include the anticyclonic structures in the Alboran Sea and Liguro-Provençal Basin, as well as the Algerian Current along the North African coast. Elevated maximum ${S_A}^{Argo}$ in the cores of cyclonic features is consistent with upward displacement of deeper, saltier waters. For instance, in the Liguro-Provençal basin, NTG, and the central-western part of CMED, the circulation patterns indicate that the method preserves the coupling between hydrographic structure and geostrophic flow (Fig.1 and 5).

In the CMED and EMED, the eastward flow through the Sicily Channel is clearly resolved, bifurcating into pathways toward the Ionian Sea. The anticyclonic Sidra Gyre and the basin-scale Levantine circulation are consistently captured. Along the Libyan coast, an intensified eastward boundary current (≈6 cm s^{-1}) is present in this dataset, extending toward the Levantine Basin and connecting with meridional currents along the eastern boundary. Additional features, including the Rhodes Gyre, the Pelops Gyre, and the northward flow along the southern Turkish coast, are also coherently represented. These patterns indicate that the method successfully captures the surface circulation associated with Atlantic Water transport across the basin.

At 1000 dbar, the circulation weakens and becomes more structured at a basin scale in good agreement with the ${S_A}^{Argo}$ distribution. In the WMED, the basin exhibits a separation into sub-regions west and

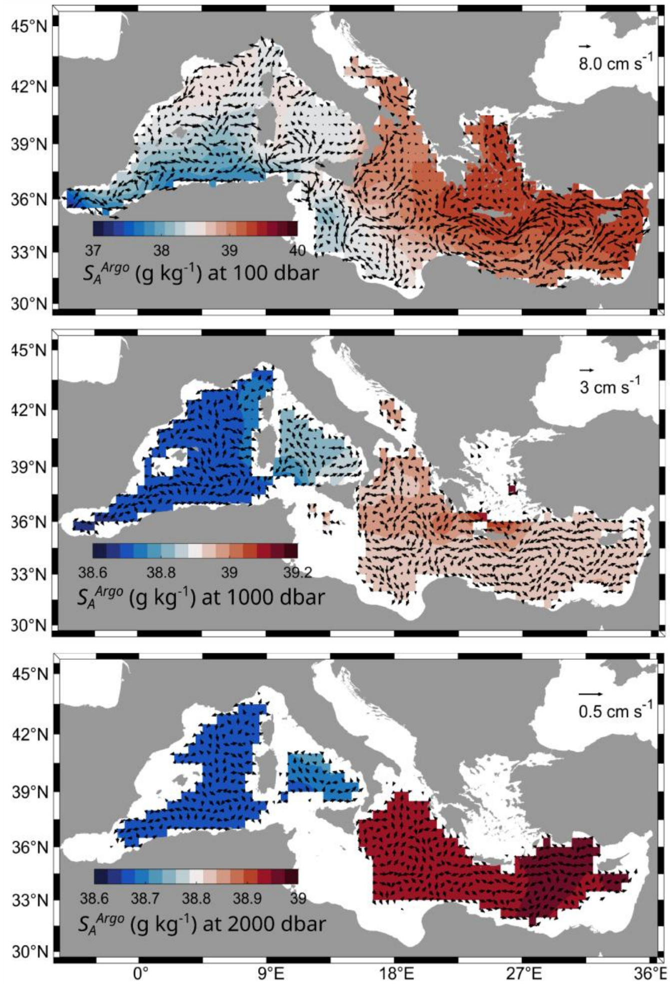

Figure 5. The map of estimated geostrophic current from the Argo Floats overlaid on $S_A{}^{Argo}$ at 100 dbar (top),1000 dbar (middle), and 2000 dbar (bottom).

https://doi.org/10.5194/essd-2026-543
Preprint. Discussion started: 4 August 2026

Open Access Earth System Science Data Discussions

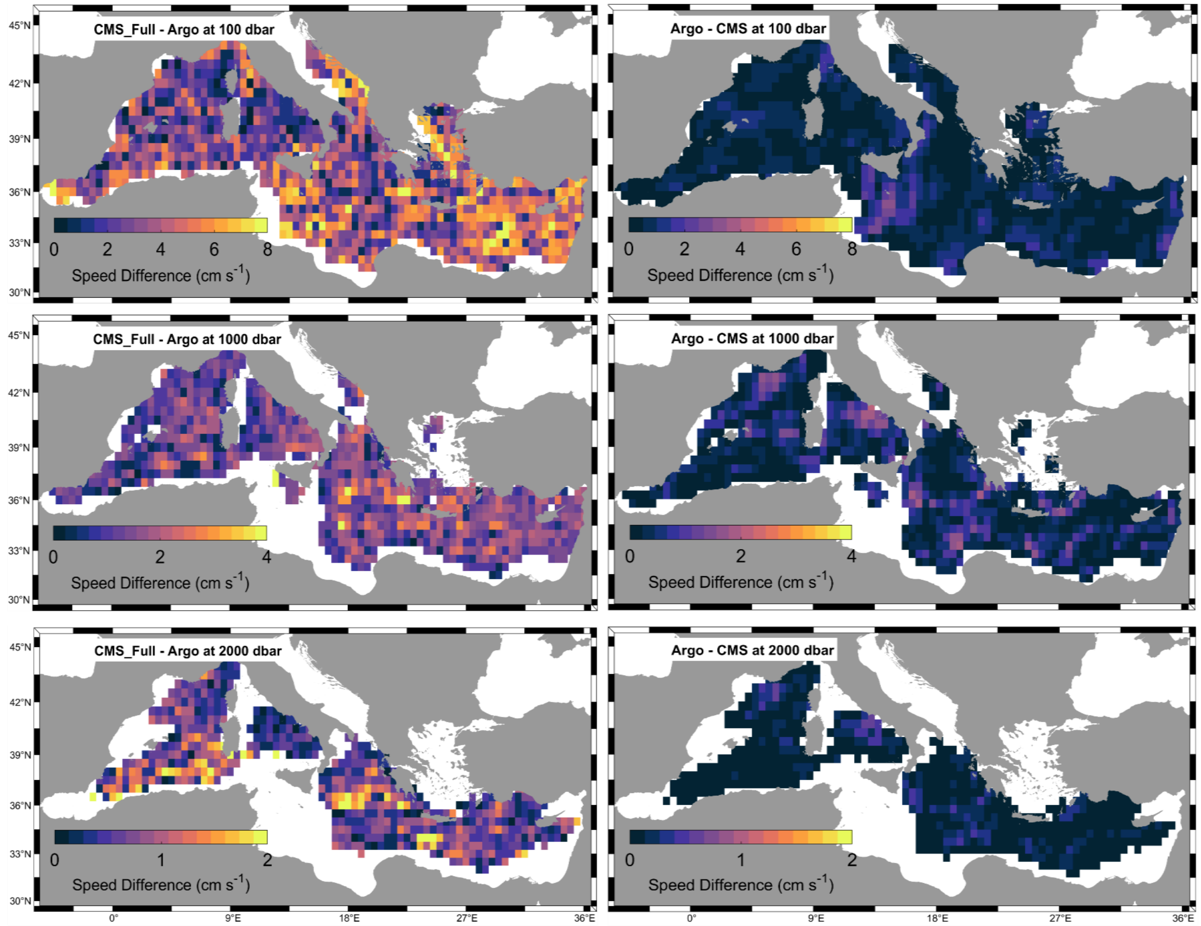

Figure 6. Difference between estimated V_g^{Argo} and V_{CMEMS_Full} in the left column, difference between V_g^{Argo} float data and V_g^{CMS} in the right column. The columns correspond to the levels at 100 dbar, 1000 dbar, and 2000 dbar, respectively.

East of Sardinia, associated with differences in $S_A{}^{Argo}$ and weaker flow magnitudes. In the CMED, the circulation is generally weak, with localized semi-anticyclonic structures, while the northern sector shows evidence of transport pathways linking the Adriatic, Ionian, and western basins. In the EMED, cyclonic circulation dominates the southern region, with weaker westward flow in the northern part. At 2000 dbar, V_g^{Argo} fields are significantly reduced (≤0.6 cm s^{-1}) across all basins. The circulation becomes more homogeneous, with weak large-scale structures influenced by deep water-mass distribution. Remarkably, the basin appears partitioned into broad regions associated with $S_A{}^{Argo}$ contrasts, although flow magnitudes remain small.

https://doi.org/10.5194/essd-2026-543
Preprint. Discussion started: 4 August 2026

The skill of the velocity reconstruction method is further evaluated using the magnitude of the vector difference between datasets as shown in Fig. 6. The top row presents differences between V_g^{Argo} and V_g^{CMS}, while the bottom row shows differences between V_g^{Argo} and V_{CMS_Full}. Columns correspond to depths of 100, 1000, and 2000 dbar.

At 100 dbar, the difference between V_g^{Argo} and V_{CMS_Full} exceeds 7 cm s$^{-1,}$ while on the other hand, the discrepancies between V_g^{Argo} and V_g^{CMS} decrease up to ~2 cm s^{-1}. These large differences are primarily concentrated along coastal regions and areas of complex bathymetry, including the Libyan coast, the Levantine Basin, the Gulf of Lion, and the Sicily Channel, where strong velocity gradients and ageostrophic processes are expected.

At 1000 dbar, differences decrease substantially. The discrepancy between V_g^{Argo} and V_g^{CMS} falls below ~0.5 cm s^{-1}, while differences with V_{CMS_Full} reduce to approximately 3.5 cm s^{-1}. Spatially, the discrepancies extend further into the basin interior, particularly in the Ionian Sea and at the boundary between the CMED and EMED.

At 2000 dbar, velocity differences are further reduced, with discrepancies between geostrophic estimates below 0.5 cm s^{-1}, and those relative to V_{CMS_Full} below ~1.5 cm s^{-1}. The remaining differences are primarily associated with the meridional component, consistent with the bias structure shown in Fig. 4. Spatially, residual discrepancies persist in dynamically active regions such as the Levantine Basin, the Gulf of Lion, and the Sicily Channel.

The larger discrepancies observed in the upper ocean may be partly attributed to ageostrophic motions represented in V_{CMS_Full}, together with enhanced variability in coastal and topographically complex regions. In Addition, the relatively sparse observational coverage in the EMED may contribute to the increased differences observed in that basin.

5. Discussion

The present study reconstructed the 3D geostrophic current fields in the Mediterranean Sea using a modified version of Vigo et al. (2018) work, along with Argo floats and altimetric data. The obtained estimates were validated using full velocity from CMS, and estimated geostrophic current velocity fields from $S_A{}^{CMS}$ and Θ_{CMS}.

https://doi.org/10.5194/essd-2026-543
Preprint. Discussion started: 4 August 2026

The results of this study demonstrate that the choice of numerical formulation significantly affects the quality of subsurface geostrophic velocity reconstructions. The anomaly-based method produced velocity profiles that decay with depth, consistent with the expected decrease in horizontal density gradients in the Mediterranean interior.

This performance arises from the vertical integration procedure. In the anomaly-based approach, the subtraction of $1/\rho_o$ from $1/\rho$ reduces: 1) the integrated hydrostatic signal that grows monotonically with depth, 2) small errors introduced during interpolation, 3) finite differencing that accumulates into spurious horizontal pressure gradients. These residual gradients amplify at depth, producing unrealistic velocities. Similar numerical sensitivities have been documented in other geostrophic reconstruction studies (Biló et al., 2014; Lankhorst & Send, 2020).

Despite these improvements, the reconstructed fields exhibit limitations in regions with sparse observational coverage. In the Adriatic Sea, southern Levantine Basin, and narrow straits such as the Sicily Channel and the Strait of Gibraltar, the geostrophic fields exhibit increased noise and fail to resolve known circulation features including the Sidra Gyre and the Atlantic-Ionian Stream. These deficiencies reflect both data sparsity and the breakdown of geostrophic assumptions in coastal and strait environments.

Future efforts should focus on integrating higher-resolution altimetric products, regional ocean models, and targeted in-situ measurements to improve reconstructions in dynamically complex regions. Such developments are essential for extending anomaly-based geostrophic methods to coastal and marginal seas where conventional approaches remain limited.

6. Conclusion

This study reconstructed three-dimensional geostrophic velocities for the Mediterranean Sea down to 2000 dbar using Argo hydrography referenced to satellite altimetry. The specific-volume anomaly method outperforms the full specific-volume approach, producing depth-decaying velocity profiles consistent with observed hydrography while avoiding numerical artifacts that cause artificial amplification of velocities in deep layers.

The reconstructed fields capture basin-scale circulation, mesoscale eddies, and boundary currents, with RMSD values relative to CMS reanalysis of ~1 cm s^{-1} above 500 dbar and O(10^{-3}) cm s^{-1} at depth. Larger

https://doi.org/10.5194/essd-2026-543
Preprint. Discussion started: 4 August 2026

Open Access Earth System Science Data Discussions

uncertainties occur between 500-1200 dbar due to thermohaline variability near water mass boundaries, and under 1200dbar the difference decreases toward zero.

Limitations arise from sparse Argo coverage in coastal regions, narrow straits, and the southern Levantine and Adriatic basins, where features such as the Sidra Gyre and Atlantic-Ionian Stream remain poorly resolved. Extending this approach to these regions will require higher-resolution observations and complementary dynamical constraints.

The dataset presented herein provides a foundation for investigating Mediterranean thermohaline variability, heat and volume transport, and changes in long-term circulation in the context of ongoing climate change. Future developments should prioritize enhanced coastal and intermediate-depth sampling, integration with high-resolution regional models, and refined interpolation techniques to improve velocity reconstructions in data-sparse and dynamically active regions.

7. Code and data availability

The Climate Data Operator (CDO) available at https://www.unidata.ucar.edu/software/netcdf/workshops/2012/third_party/CDO.html was used to remap the data from the original horizontal resolution to the resolution of 0.5 ° × 0.5 ° used in this study, and maps were prepared using the cartopy package, which is available at https://cartopy.readthedocs.io/stable/. Python codes that were used for data preprocessing and numerical computation can be accessed upon request to the authors. The dataset produced by this work is archived at the National Oceanographic Data Center of the National Institute for Oceanography and Applied Geophysics (NODC-OGS), Italy, and is available at https://doi.org/10.13120/q25v-q872 and will be cited as (Manimipire Gasana et al., 2026).

Author contributions. MGE, MM and AP conceptualised the study and conducted the investigation. MGE, RM and AG curated and validated the data. MGE prepared the first draft of the manuscript and produced the results. PMP, MGE, MM, AP and MG defined the methodology and contributed to the interpretation of results. EM acquired funding and supervised the study. All authors reviewed and edited the manuscript.

Competing interests. The authors declare that they have no conflict of interest.

Disclaimer. There is no guarantee that the product is error-free. The data users are responsible for the preparation of the required product and interpretation according to individual tasks.

Acknowledgement. This research was funded by the Italian Ministry of University and Research as part of the ARGO-ITALY program. Argo float data were collected and made freely available by the International Argo Program and the national programs that contribute to it. (https://argo.ucsd.edu, https://www.ocean-ops.org). The Argo Program is a part of the Global Ocean Observing System.

References

Alvarez, A., Chiggiato, J., & Schroeder, K. (2013). Mapping sub-surface geostrophic currents from altimetry and a fleet of gliders. *Deep-Sea Research Part I: Oceanographic Research Papers*, 74, 115–129.

Biló, T. C., da Silveira, I. C. A., Belo, W. C., de Castro, B. M., & Piola, A. R. (2014). Methods for estimating the velocities of the Brazil Current in the pre-salt reservoir area off southeast Brazil (23°S–26°S). *Ocean Dynamics, 64*, 1431–1446. https://doi.org/10.1007/s10236-014-0761-2.

Cocks, J., Silvano, A., Naveira Garabato, A. C., Dragomir, O., Schifano, N., Hogg, A. E., & Marzocchi, A. (2025). Satellite-derived steric height in the Southern Ocean: Trends, variability, and climate drivers. *Ocean Science, 21*, 1609–1625. https://doi.org/10.5194/os-21-1609-2025

Doglioni, F., Ricker, R., Rabe, B., Barth, A., Troupin, C., & Kanzow, T. (2023). *Sea surface height anomaly and geostrophic current velocity from altimetry measurements over the Arctic Ocean (2011–2020)*. **Earth System Science Data, 15**(1), 225–263. https://doi.org/10.5194/essd-15-225-2023.

Estournel, C., Marsaleix, P., & Ulses, C. (2021). A new assessment of the circulation of Atlantic and Intermediate Waters in the Eastern Mediterranean. *Progress in Oceanography, 198*, 102673. https://doi.org/10.1016/j.pocean.2021.102673.

Ferrari, R., & Wunsch, C. (2009). Ocean Circulation Kinetic Energy: Reservoirs, Sources, and Sinks. *Annual Review of Fluid Mechanics*, 41, 253–282.

Gill, A. E. (1982). *Atmosphere–ocean dynamics*. Academic Press.

Groeskamp, S. (2015). *Diagnosing the relation between ocean circulation, mixing and water-mass transformation from an ocean hydrography and air-sea fluxes* (Doctoral dissertation, University of Tasmania).

Malanotte-Rizzoli, P., Manca, B. B., Ribera d'Alcalà, M., Theocharis, A., Bergamasco, A., Bregant, D., Budillon, G., Civitarese, G., Georgopoulos, D., Michelato, A., Sansone, E., Scarazzato, P., & Souvermezoglou, E. (1997). A synthesis of the Ionian Sea hydrography, circulation and water mass pathways during POEM-Phase I. *Progress in Oceanography, 39*(3), 153–204. https://doi.org/10.1016/S0079-6611(97)00013-X.

Manimpire Gasana E., Pirro A., Mauri E., Martellucci R., Gallo A., Bussani A., Notarstefano G., Gačić M., Poulain P.-M., and Menna M. (2026) **Geostrophic Currents in the Mediterranean Sea (0–2000 m) derived from Argo float observations**. https://doi.org/10.13120/q25v-q872.

McDougall, T. J., Barker, P. M., Holmes, R. M., Pawlowicz, R., Griffies, S. M., & Durack, P. J. (2021). The interpretation of temperature and salinity variables in numerical ocean model output and the calculation of heat fluxes and heat content. *Geoscientific Model Development*, *14*(10). https://doi.org/10.5194/gmd-14-6445-2021.

Menna, M., & Poulain, P. M. (2010). Mediterranean intermediate circulation estimated from Argo data in 2003–2010. *Ocean Science, 6*(2), 331–343. https://doi.org/10.5194/os-6-331-2010.

Menna, M., Reyes Suarez, N. C., Civitarese, G., Gačić, M., Rubino, A., & Poulain, P.-M. (2019). *Decadal variations of circulation in the Central Mediterranean and its interactions with mesoscale gyres*. Deep Sea Research Part II: Topical Studies in Oceanography, 164, 14–24. https://doi.org/10.1016/j.dsr2.2019.02.004

Menna, M., Gačić, M., Martellucci, R., Notarstefano, G., Mauri, E., Gerin, R., & Poulain, P. M. (2022). Climatic, decadal, and interannual variability in the upper layer of the Mediterranean Sea using remotely sensed and in-situ data. *Remote Sensing, 14*(4), 1322. https://doi.org/10.3390/rs14041322

Millot, C. (2005). Circulation in the Mediterranean Sea : evidence. *Circulation*, *69*(Suppl. 1).

Mulet, S., Rio, M. H., Mignot, A., Guinehut, S., & Morrow, R. (2012a). A new estimate of the global 3D geostrophic ocean circulation based on satellite data and in-situ measurements. *Deep-Sea Research Part II: Topical Studies in Oceanography*, *77–80*, 70–81. https://doi.org/10.1016/j.dsr2.2012.04.012.

Mulet, S., et al. (2024). Quality Information Document for Multi-Observations Global Ocean ARMOR3D L4 Analysis. Copernicus Marine Environment Monitoring Service (CMEMS).

Napolitano, E., Carillo, A., Struglia, M. V., Iacono, R., Palma, M., Eusebi Borzelli, G. L., & Sannino, G. (2025). *The role of the Atlantic-Ionian stream in the long-term variability of the surface circulation in the Northern Ionian Sea: Results from a hindcast simulation*. Progress in Oceanography, 234, 103472. https://doi.org/10.1016/j.pocean.2025.103472

Patterson, M., O'Reilly, C., Robson, J., & Woollings, T. (2024). Disentangling North Atlantic Ocean–Atmosphere Coupling Using Circulation Analogs. *Journal of Climate*, *37*(14), 3791-3805.

Poulain, P.-M., Menna, M., & Mauri, E. (2012). *Surface geostrophic circulation of the Mediterranean Sea derived from drifter and satellite altimeter data*. Journal of Physical Oceanography, 42(6), 975–990. https://doi.org/10.1175/JPO-D-11-0159.1

Rio, M. H., Pascual, A., Poulain, P. M., Menna, M., Barceló, B., & Tintoré, J. (2014). Computation of a new mean dynamic topography for the Mediterranean Sea from model outputs, altimeter measurements and oceanographic in situ data. *Ocean Science*, *10*(4), 731–744. https://doi.org/10.5194/os-10-731-2014 .

Riser, S. C., Freeland, H. J., Roemmich, D., Wijffels, S., Troisi, A., Belbéoch, M., Gilbert, D., Xu, J., Pouliquen, S., Ann Thresher, S. E., Le Traon, P. Y., Maze, G., Klein, B., Ravichandran, M., Grant, F., Poulain, P. M., Suga, T., Lim, B., Sterl, A., ... Owens, W. B. (2016). Fifteen years of ocean observations with the global Argo array. *Nature Climate Change, 6*(2), 145–153. https://doi.org/10.1038/nclimate2872.

Robinson, A. R., Leslie, W. G., Theocharis, A., & Lascaratos, A. (2001). *Mediterranean Sea circulation*. In J. H. Steele, S. A. Thorpe, & K. K. Turekian (Eds.), **Encyclopedia of Ocean Sciences** (pp. 1689–1705). Academic Press. https://doi.org/10.1006/rwos.2001.0376

https://doi.org/10.5194/essd-2026-543
Preprint. Discussion started: 4 August 2026

Schmitz, W. J. (1995). On the interbasin-scale thermohaline circulation. *Reviews of Geophysics, 33*(2), 151-173. https://doi.org/10.1029/95RG00879.

Vargas-Alemañy, J. A., Vigo, M. I., García-García, D., & Zid, F. (2023). Updated geostrophic circulation and volume transport from satellite data in the Southern Ocean. *Frontiers in Earth Science*, *11*. https://doi.org/10.3389/feart.2023.1110138.

Vigo, M. I., García-García, D., Sempere, M. D., & Chao, B. F. (2018). 3D geostrophy and volume transport in the Southern Ocean. *Remote Sensing*, *10*(5). https://doi.org/10.3390/rs10050715 .

Wunsch, C. (1997). The vertical partition of oceanic horizontal kinetic energy. *Journal of Physical Oceanography*, 27(8), 1770–1794.